THYROID
Volume 27, Number 11, 2017

DOI: 10.1089/thy.2017.0264

Automated MicroSPECT/MicroCT Image Analysis of the Mouse Thyroid Gland

Peng Cheng,[1,*] Brynn Hollingsworth,[2,*] Daniel Scarberry,[2] Daniel H. Shen,[3] Kimerly Powell,[4] Sean C. Smart,[5] John Beech,[5] Xiaochao Sheng,[1] Lawrence S. Kirschner,[6] Chia-Hsiang Menq,[1] and Sissy M. Jhiang[2]

Background: The ability of thyroid follicular cells to take up iodine enables the use of radioactive iodine (RAI) for imaging and targeted killing of RAI-avid thyroid cancer following thyroidectomy. To facilitate identifying novel strategies to improve ^{131}I therapeutic efficacy for patients with RAI refractory disease, it is desired to optimize image acquisition and analysis for preclinical mouse models of thyroid cancer.
Methods: A customized mouse cradle was designed and used for microSPECT/CT image acquisition at 1 hour (t1) and 24 hours (t24) post injection of ^{123}I, which mainly reflect RAI influx/efflux equilibrium and RAI retention in the thyroid, respectively. FVB/N mice with normal thyroid glands and TgBRAF^{V600E} mice with thyroid tumors were imaged. In-house CTViewer software was developed to streamline image analysis with new capabilities, along with display of 3D voxel-based ^{123}I gamma photon intensity in MATLAB.
Results: The customized mouse cradle facilitates consistent tissue configuration among image acquisitions such that rigid body registration can be applied to align serial images of the same mouse via the in-house CTViewer software. CTViewer is designed specifically to streamline SPECT/CT image analysis with functions tailored to quantify thyroid radioiodine uptake. Automatic segmentation of thyroid volumes of interest (VOI) from adjacent salivary glands in t1 images is enabled by superimposing the thyroid VOI from the t24 image onto the corresponding aligned t1 image. The extent of heterogeneity in ^{123}I accumulation within thyroid VOIs can be visualized by 3D display of voxel-based ^{123}I gamma photon intensity.
Conclusions: MicroSPECT/CT image acquisition and analysis for thyroidal RAI uptake is greatly improved by the cradle and the CTViewer software, respectively. Furthermore, the approach of superimposing thyroid VOIs from t24 images to select thyroid VOIs on corresponding aligned t1 images can be applied to studies in which the target tissue has differential radiotracer retention from surrounding tissues.

Keywords: thyroid, SPECT, CT, cradle, mouse, radioiodine

Introduction

The unique ability of thyroid follicular cells to take up iodine enables the use of radioactive iodine (RAI) for imaging and targeted killing of RAI-avid residual and metastatic thyroid cancer following thyroidectomy. The gamma ray emitting ^{123}I and the positron emitting ^{124}I are used for identifying RAI-avid lesions by single photon emission computed tomography (SPECT) and positron emission tomography (PET) imaging, respectively. After confirming RAI-avid disease by diagnostic scan, ^{131}I is administered to patients, as the beta particles emitted from ^{131}I selectively kill RAI-avid cells and nearby cells. The concomitantly emitted gamma rays from ^{131}I allow post-therapeutic imaging of RAI-avid lesions.

^{131}I therapy has proven to be effective in improving overall survival (1,2), especially for patients with RAI-avid micrometastases. However, patients with structurally discrete RAI-avid metastatic disease often require multiple ^{131}I treatments. Yet, the patients may still have persistent disease. Furthermore, patients with non-RAI-avid disease do not benefit from ^{131}I therapy, as their tumors have lost the ability to take up ^{131}I. These patients are in need of novel treatments, as their tumors are generally resistant to conventional chemotherapy (3). To date, no novel treatment has shown improved overall survival for patients with progressive RAI refractory disease,

Departments of [1]Mechanical and Aerospace Engineering, [2]Physiology and Cell Biology, [4]Biomedical Informatics, and [6]Internal Medicine, The Ohio State University, Columbus, Ohio.
[3]PET Center and Department of Nuclear Medicine, Tri-Service General Hospital, National Defense Medical Center, Taipei, Taiwan.
[5]Department of Oncology, University of Oxford, Oxford, United Kingdom.
*These authors contributed equally to this work.

despite improved progression-free survival with manageable adverse effects in some patients treated with emerging small molecule inhibitor therapy (4–6). For patients with progressive RAI refractory disease, much effort has been focused on restoring and increasing RAI uptake to improve ^{131}I therapeutic efficacy. Recently, the MEK inhibitors selumetinib and CKI were shown to increase RAI uptake in thyroid tumors via nuclear imaging in preclinical thyroid tumor mouse models (7,8). Shortly thereafter, selumetinib was shown to restore/enhance the tumoral RAI uptake in 12/20 thyroid cancer patients with RAI refractory disease (9).

To identify novel agents and to optimize dosing regimens that further increase RAI uptake, it is desired to optimize the workflow of image acquisition and enhance the capability of image analysis for thyroid cancer mouse models. This study developed a mouse cradle to achieve consistent tissue configuration of the head and neck region during image acquisition, which greatly facilitated subsequent image analysis. In-house CTViewer software was developed with the objective of streamlining image analysis with new capabilities. This enabled automatic segmentation of thyroid volumes of interest (VOI) to be conducted in SPECT/X-ray computed tomography (CT) images acquired 1 hour (t1) and 24 hours (t24) post injection of ^{123}I, which mainly reflect radioiodine influx/efflux equilibrium and radioiodine retention, respectively. In addition, it enabled *xyz* coordinates of areas with differential gamma photon intensity from ^{123}I accumulation to be identified such that the extent of heterogeneity of ^{123}I accumulation within the thyroid VOI could be evaluated.

Materials and Methods

Animals

All studies were approved by The Ohio State University's Institutional Animal Care and Use Committee, which oversees the responsible use of animals in university research and instructional activities. All research activities conformed to the statutes of the Animal Welfare Act and the guidelines of the Public Health Service as issued in the Guide for the Care and Use of Laboratory Animals. Mice used for microSPECT/CT imaging in this study include FVB/N mice and TgBRAF^{V600E} mice (10). For TgBRAF^{V600E} mice, the expression of human *BRAF^{V600E}* cDNA was targeted to thyroid cells of transgenic FVB/N mice with a bovine thyroglobulin promoter (bTg). Since *BRAF^{V600E}* expression leads to thyroid dedifferentiation and bTg promoter activity is decreased by thyroid dedifferentiation, bTg promoter-driven *BRAF^{V600E}* expression is self-limiting in TgBRAF^{V600E} mice. TgBRAF^{V600E} mice appeared to compensate successfully for thyroid dysfunction, as their serum thyroxine/triiodothyronine and somatic growth were normal (10).

Cradle design and mouse placement in cradle

To facilitate consistent positioning and tissue configuration of the mouse head and neck where the thyroid is located among image acquisitions, a cradle comprised of a jig with a groove for a gas anesthesia tube, a tooth bar, two cheek bars, and a cover with a holder for an Eppendorf tube containing known radioactivity for decay control was designed (Fig. 1A). The cradle components were printed using RDG720 material with an Objet Prime 30 3D printer (Stratasys, Eden Prairie, MN) at 0.0006 inch resolution, and were assembled and attached to the mouse bed in the Flex-XO SPECT/CT system (TriFoil Imaging, Inc., Chatsworth, CA) using nylon screws and fasteners so as not to distort the X-ray CT image. The jig serves as a base for all cradle parts. The tooth bar holds the top incisors of the mouse to maintain the head position in the cranial/caudal direction. The cheek bars are placed on either side of the mouse head to maintain the head position in the right/left direction. The cover traps gas anesthesia inside of the cradle to ensure the mouse remains unconscious and holds an Eppendorf tube containing known radioactivity for decay control. The components of the cradle relative to the mouse being imaged are shown in Figure 1B–D.

For mouse placement in the cradle, the mouse first has its top incisors positioned in the hole of tooth bar. The limbs are placed on the outside of the cradle, and the body is positioned symmetrically in the right/left direction. The tail is gently pulled back to straighten the spine, the cheek bars are placed against the mouse, and the cover is placed on the jig (Supplementary Video S1; Supplementary Data are available online at www.liebertpub.com/thy).

MicroSPECT/CT image acquisition

All mice subjected to microSPECT/CT imaging were intraperitoneally injected with 400–450 μCi of ^{123}I or 185–250 μCi of $^{99m}TcO_4^-$ in 200 μL of saline prepared by the nuclear pharmacy at the authors' institute. Radioactivity was measured by a dose calibrator (CRC-12; Capintec, Florham Park, NJ) and normalized for radioactive decay. The mouse was anesthetized with 4% isoflurane mixed with O_2 at a flow rate of 1.5 L/min for 3 min and then placed in the cradle with 1.5–2% isoflurane mixed with O_2 at the same flow rate. A 0.25 mL Eppendorf tube containing 10–30 μCi of ^{123}I was included as a decay control. Image acquisition was conducted at 1 h (t1) and 24 h (t24) after ^{123}I injection or 1 h after $^{99m}TcO_4^-$ injection. Mice imaged with $^{99m}TcO_4^-$ were imaged multiple times, and these images were used for mouse rotation and translation analyses. SPECT images were acquired with two gamma cameras equipped with 1 mm single-pinhole collimators (75 mm focal distance) using the following settings: 180° rotation per camera, 32 projections per camera, 30 s projection duration, and 30 mm radius of rotation. CT images were acquired with a single X-ray detector camera at the following settings: X-ray tube set to 75 kVp, 360° rotation, 1024 projections, one frame per projection, and 2.5× magnification. The SPECT image is $80\times80\times80$ pixels, with a resolution of 0.52 mm, while the CT image is $512\times512\times512$ pixels with a resolution of 0.075 mm.

Image analysis with in-house CTViewer software

A Microsoft foundation class (MFC)-based CT and SPECT image analysis software, CTViewer, was designed in-house, in which all the algorithms for image processing and data analysis were written in C++. The capabilities of CTViewer include (i) loading RAW data sets of SPECT and CT images; (ii) co-registering SPECT and CT images based on the pre-calibrated coordinate transformation; (iii) displaying the SPECT and CT images in three orthogonal planes, whether separately or in fusion mode; (iv) automatically selecting VOIs in a threshold-based manner; and (v) automatically calculating percentage of injected radioisotope in thyroid VOIs. In addition

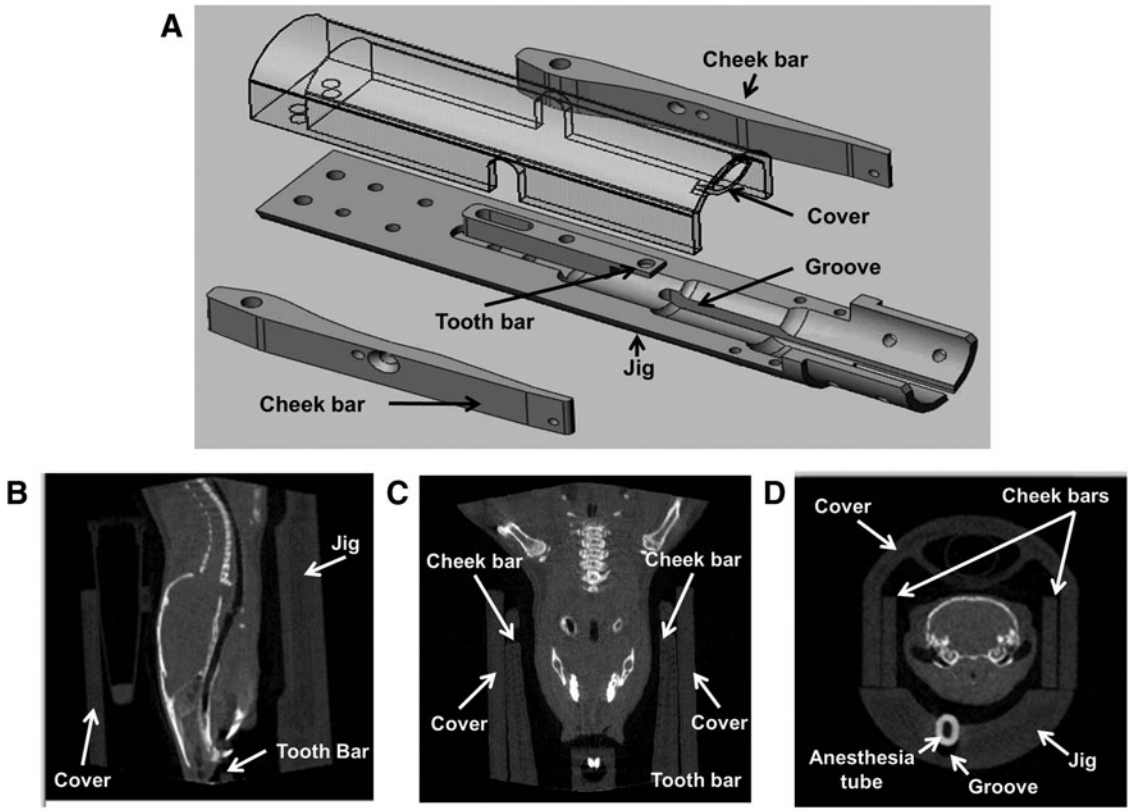

FIG. 1. Cradle design and X-ray computed tomography image of mouse in cradle. (**A**) Computer-aided design of the mouse cradle components: a jig with groove for a gas anesthesia tube, a tooth bar with a hole to anchor the mouse's top incisors, two cheek bars, and a cover with holder for an Eppendorf tube containing decay control of known radioactivity. (**B**–**D**) X-ray computed tomography (CT) image of a mouse in the cradle in sagittal view (**B**), coronal view (**C**), and transaxial view (**D**).

to the aforementioned capabilities, a two-step rigid body registration was developed to align images of the same mice taken at different times. First, CTViewer coarsely aligns the target CT image to the reference CT image based on the skull (the rigid body) using principle component analysis and iteratively adjusting VOIs. In the second step, the two CT images are finely aligned using 3D image correlation in three iterations. Consequently, the computation time is greatly reduced. The same coordinate transformation matrix is then applied to align the corresponding two SPECT images. The features of CTViewer and the time required for the whole process are shown in Supplementary Video S2.

Results

Cradle-enabling pose control leading to consistent tissue configuration

Due to a living mouse's body being flexible, the spatial relationship between target tissues of interest and surrounding anatomic landmarks varies significantly among images acquired on a standard CT imaging bed. As shown in Figure 2, consistency of tissue configuration within the head and neck region is greatly improved when the cradle is employed. To evaluate the effectiveness of the cradle in achieving pose control, translation and rotation required to align two images acquired at different times, such as t1 and t24, were calculated for each individual mouse. This process was applied to four FVB/N mice and six TgBRAF^{V600E} mice. The sagittal (x), coronal (y), and transaxial (z) translation and the rotation around x, y, and z axes of these 14 mice are summarized in Table 1. Regardless of the difference in age (4.8–16.7 months), body weight (19.9–45 g), mouse model, and between two users, the x, y, and z translations for all mice are <1 mm. The rotation around the x and y axes for all mice are <5°. The rotation around the z axis has the greatest variability, yet is <11°.

Automatic segmentation of thyroid VOIs on t1 and t24 SPECT images

At 1 h post ^{123}I injection, ^{123}I accumulates not only in the thyroid gland but also in the salivary glands as both glands express the Na^+/I^- symporter, which mediates ^{123}I influx against its concentration gradient. The mouse thyroid and salivary glands are in close proximity, and the boundaries of soft tissues are not discernable via the anatomical CT image. It is therefore difficult to separate ^{123}I accumulation in the thyroid gland from adjacent salivary glands in t1 SPECT images. At 24 h post ^{123}I injection, ^{123}I has been organified into thyroglobulin and retained in the thyroid, whereas ^{123}I in the salivary gland is not retained. Consequently, ^{123}I accumulation in the thyroid gland is readily discernable in t24 SPECT images, and the thyroid VOI can be automatically segmented in a threshold-based manner. After t1 and t24 images are aligned, the thyroid VOI from the t24 image can

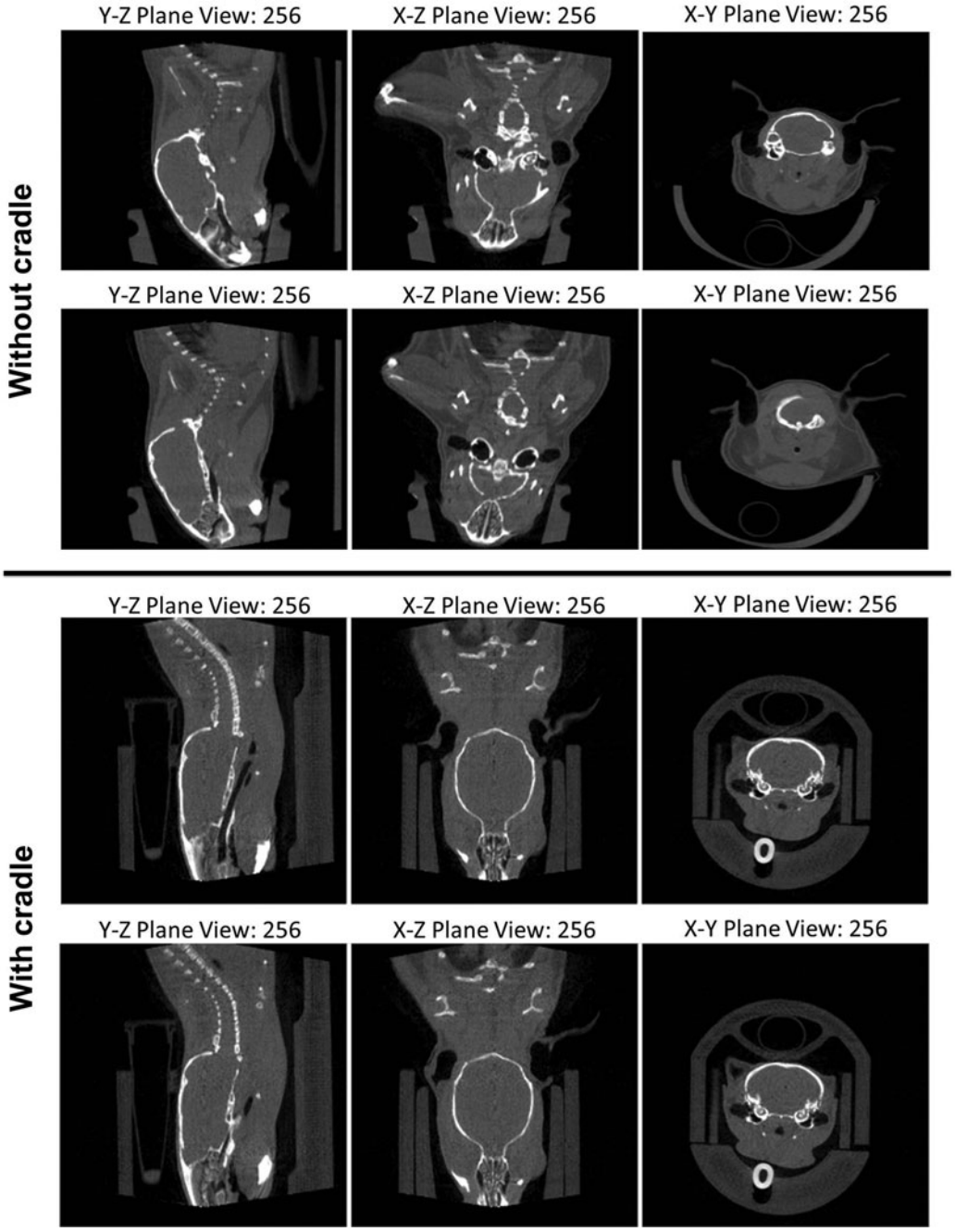

FIG. 2. Tissue configuration variation in head and neck region is greatly reduced with the use of cradle during image acquisition. The top two rows show the sagittal, coronal, and transaxial views of X-ray CT images of the same mouse acquired on separate days without the cradle. The bottom two rows show the sagittal, coronal, and transaxial views of CT images of the same mouse acquired on separate days with the cradle.

TABLE 1. MOUSE POSITIONING CONSISTENCY BETWEEN SERIAL IMAGES OF INDIVIDUAL MICE

	FVB/N (n = *4*)	*TgBRAF*^{V600E} (n = *3*)	*TgBRAF*^{V600E} [a] (n = *3*)
x-axis rotation (degrees)	1.33 ± 0.68	1.05 ± 0.80	2.60 ± 1.34
y-axis rotation (degrees)	1.71 ± 1.74	1.68 ± 1.63	1.00 ± 1.05
z-axis rotation (degrees)	6.30 ± 3.15	1.42 ± 0.22	2.21 ± 2.64
x translation (mm)	0.22 ± 0.24	0.36 ± 0.33	0.19 ± 0.24
y translation (mm)	0.37 ± 0.21	0.21 ± 0.15	0.58 ± 0.19
z translation (mm)	0.14 ± 0.11	0.09 ± 0.06	0.46 ± 0.41

The translation and rotation between images for each mouse model are presented as mean ± standard deviation.
[a]Mouse placement in the cradle and subsequent imaging conducted by the second user.

be superimposed onto the t1 image to enable automatic segmentation of t1 thyroid VOI. The CT images of t1 and t24 prior to and after alignment are shown in Figure 3A versus 3D (sagittal view), 3B versus 3E (transaxial view), and 3C versus 3F (coronal). Automatic segmentation of the thyroid VOI in t24 image is shown in Figure 3G–I, wherein the perimeter of VOI is indicated with a red curve. The perimeter of t24 thyroid VOI is then superimposed onto the aligned t1 image, as shown in Figure 3J–L. It can be seen that the red curve encloses the region with highest gamma photon intensity from ^{123}I, the anticipated thyroid VOI of the t1 image. This demonstrates the effectiveness of pose control using the cradle and the accuracy of image alignment. Taken together, the cradle along with the in-house CTViewer software allows the thyroid VOI to be automatically defined in t1 and t24 SPECT images without user subjectivity.

Evaluating the extent of ^{123}I uptake heterogeneity within the thyroid via 3D voxel-based ^{123}I gamma photon intensity

MicroSPECT/CT imaging is used to locate tissues accumulating radioisotope tracer and quantify their radioisotope tracer uptake. Heterogeneity of radioisotope tracer uptake within target tissues of interest is rarely quantitatively evaluated. It is known that thyroid cancer patients with RAI-avid lesions of larger size are less responsive to ^{131}I therapy. One could assume that ^{131}I uptake in larger metastatic lesions would have a greater extent of heterogeneity in ^{131}I uptake such that areas with insufficient ^{131}I uptake would escape from ^{131}I therapeutic effect. To investigate the effects of heterogeneity on ^{131}I therapeutic efficacy, it must be possible to evaluate quantitatively the extent of ^{131}I uptake heterogeneity within lesions of interest. The current CTViewer does not have the capability of 3D display.

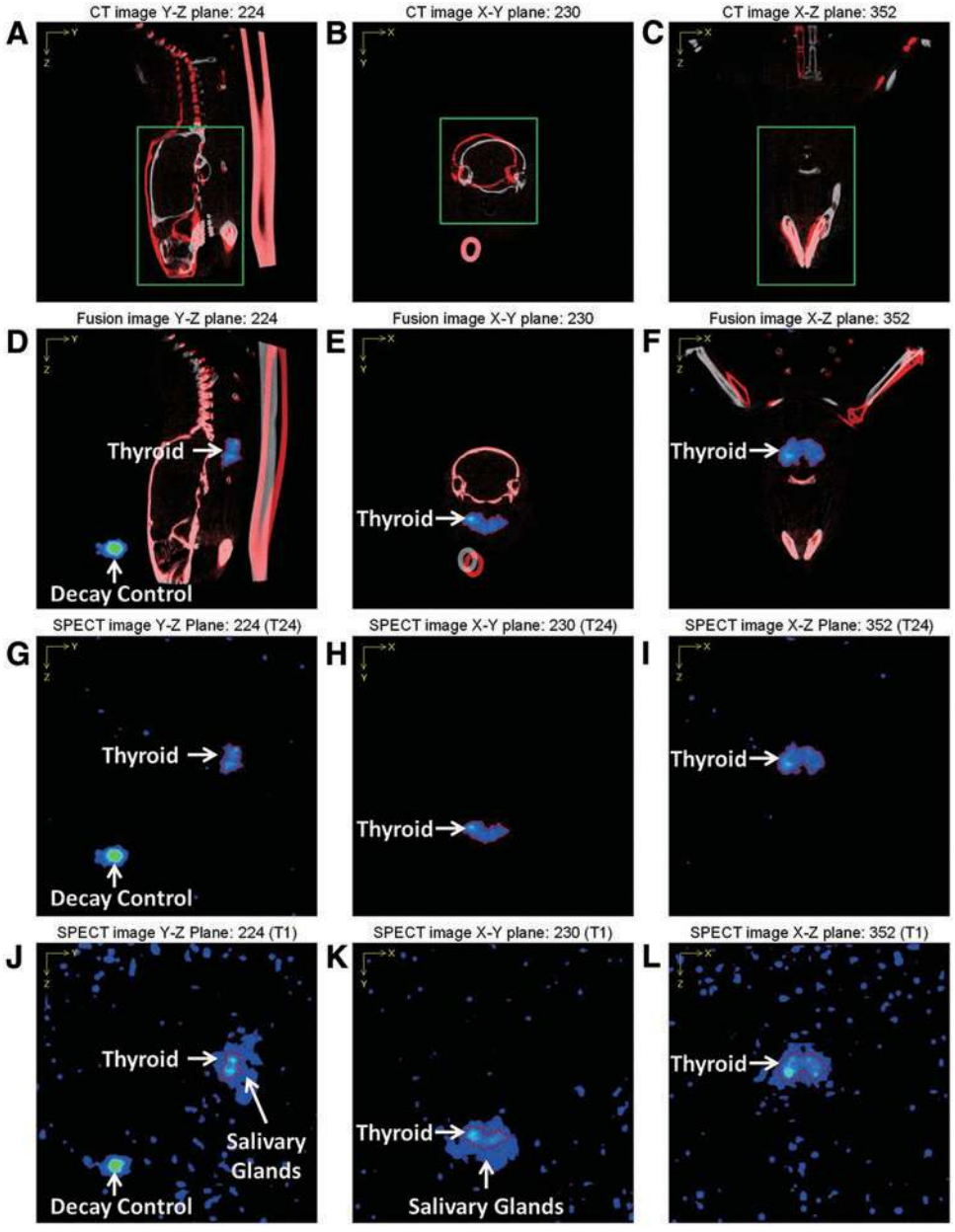

FIG. 3. Automatic segmentation of thyroid volume of interest (VOI) on t1 image via superimposing thyroid VOI from t24 SPECT image. MicroSPECT/CT images are acquired at 1 h (t1) and 24 h (t24) post ^{123}I injection. The sagittal (**A** and **D**), transaxial (**B** and **E**), and coronal (**C** and **F**) views of a t1 CT image (shown in red) and a t24 CT image (shown in white) prior to (**A**–**C**) and after (**D**–**F**) alignment are shown. (**G**–**I**) The sagittal (**G**), transaxial (**H**), and coronal (**I**) views of the thyroid VOI (perimeter in red) on the t24 SPECT image. (**J**–**L**) The sagittal (**J**), transaxial (**K**), and coronal (**L**) views of the thyroid VOI from the t24 image (perimeter in red) superimposed on the t1 SPECT image. The decay control is also shown in (**D**), (**G**), and (**J**). Color images available online at www.liebertpub.com/thy

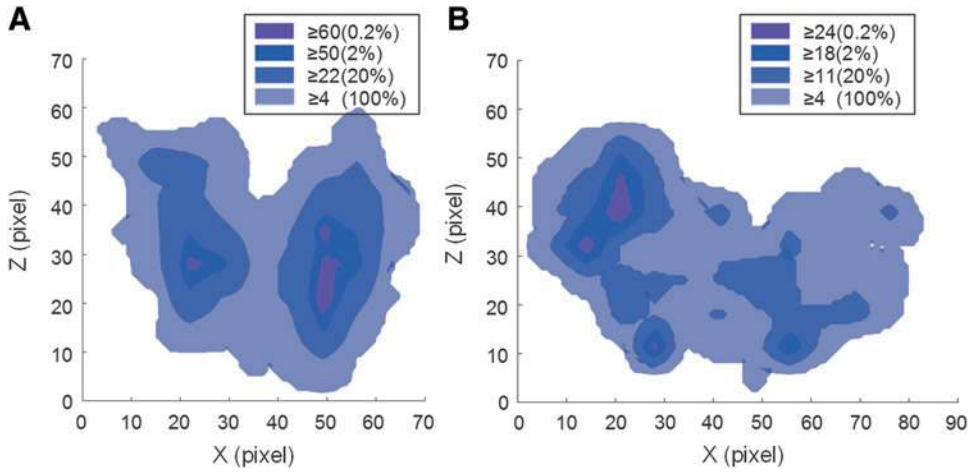

FIG. 4. Coronal view of 3D voxel-based gamma photon intensity of a FVB/N mouse thyroid (**A**) and a TgBRAF^{V600E} mouse thyroid tumor (**B**). The 3D contour of the thyroid volume of interest (VOI) was segmented using a threshold of 4 in the image taken 24 h post ^{123}I injection. Spatial heterogeneity of gamma photon intensity within the thyroid VOI is shown by further segmentation of regions with threshold values corresponding to 20%, 2%, and 0.2% of the VOI voxels. Color images available online at www.liebertpub.com/thy

The 3D data sets of the thyroid VOI in the SPECT image were exported and loaded into MATLAB to display 3D voxel-based ^{123}I gamma photon intensity. Accordingly, the spatial distribution of areas with different levels of gamma photon intensity can be visualized and analyzed.

In normal thyroid VOI of FVB/N mice (Fig. 4, left panel, and Supplementary Video S3), the center of both thyroid lobes had the highest level of ^{123}I accumulation, indicating a higher metabolic activity and an increased iodinating capacity of centrally located small follicles. Follicles located peripherally are usually composed of flattened follicular epithelium that surrounds big colloids with low turnover rate and a reduced iodinating capacity.

In thyroid tumor VOI of TgBRAF^{V600E} mice (Fig. 4, right panel, and Supplementary Video S4), the spatial distribution of heterogeneity in ^{123}I accumulation was asymmetric between thyroid lobes and had many areas with low ^{123}I accumulation. As shown in Figure 4, gamma photon intensity in normal thyroid is much higher than *BRAF^{V600E}*-driven thyroid tumors, with the top 2% of normal thyroid voxels having gamma photon intensity ≥50, while the top 2% of thyroid tumor voxels had a gamma photon intensity ≥18. Sixteen additional TgBRAF^{V600E} mice were investigated, which were five months of age. Their ^{123}I uptake was asymmetric between two thyroid lobes, and the extent of heterogeneity in ^{123}I uptake within thyroid tumor varied greatly among these age-matched mice. Identifying the location and quantifying the volume of areas with high or low gamma photon intensity will help to explain and predict differential response to ^{131}I therapy among ^{131}I-avid lesions.

Discussion

This study utilized a mouse cradle during image acquisition to achieve consistent tissue configuration within the head and neck region. This allowed rigid body registration to be applied to align serial images taken at different times of the same subject mice with accuracy. Automatic segmentation of thyroid VOIs in t1 images is enabled by superimposing thyroid VOIs from the t24 images onto their corresponding aligned t1 images. Based on 3D voxel-based ^{123}I gamma photon intensity, it is possible to evaluate the extent of heterogeneity of ^{123}I uptake within thyroid VOIs in terms of spatial distance and volume of areas with high or low gamma photon intensity. These advances will greatly facilitate the effort to uncover novel strategies to improve ^{131}I therapeutic efficacy.

Cradles have been routinely used to facilitate the accuracy of cranial irradiation in small animals (11–14) or co-registration of multimodality and longitudinal images (15–18). Among various cradles for the mouse head and neck region, the tooth bar anchoring upper incisors is essential. Ear bars (13,18) are effective but are difficult to use, leading to the use of alternatives such as a Styrofoam neck collar (11) or cheek bars in the cradle used in this study. With 3D printing technology, cradles can be easily customized and produced at low cost. For studies requiring consistency in tissue configuration, use of a cradle during image acquisition is necessary. Consistent tissue configuration allows rigid body registration among serial images of the same mice to correct any difference in position and orientation post-image acquisition easily. It is hoped that these studies will encourage cradles to be used widely among investigators.

VOI selection for targets with discrete signal in functional images is not problematic. VOI selection for multiple targets with close physical proximity in functional images requires co-registration of anatomic images that show discernable boundaries between targets. The boundaries of soft tissues are usually not discernable without contrast agent in CT images. While magnetic resonance imaging (MRI) is superior to CT imaging in visualizing the boundaries of soft tissues, MRI is time consuming, costly, and not widely available. Alternatively, the 3D MOBY digital mouse phantom (19) has been used as a common reference to facilitate VOI selection in functional images (20,21). However, this approach is less accurate, as the proportion of the target tissues to the rest of the mouse body may be different between subject mice and the mouse phantom. Most importantly, this approach cannot be applied to tumors with varying size and shape.

The fact that thyroid tissue has a discrete signal on the t24 image due to its unique ability to retain radioiodine allows automatic segmentation of the thyroid VOI in the t24 image to be conducted in a threshold-based manner. The thyroid VOI from the t24 image can then be superimposed onto its corresponding aligned t1 image to select the thyroid VOI in the t1 image automatically. In this study, consistent tissue configuration facilitated by the use of a cradle during image acquisition allowed the head and neck region to be treated as a rigid body, such that anatomic landmarks could be used for alignment of serial images by rigid body registration. While deformable registration is a powerful avenue to align images (20,22), the need to compensate difference in tissue configuration between images may lead to changes in voxel-based geometry of target tissues. Taken together, this approach can be applied to studies in which target tissue has differential radiotracer retention from surrounding tissues.

The overall response to ^{131}I therapy is likely limited by the volume of areas with insufficient ^{131}I accumulation (23). It is reasoned that insufficient ^{131}I accumulation in micro-foci would have less impact than macro-foci on overall therapeutic outcome due to possible bystander effects of ^{131}I. The 3D data set of voxel-based gamma photon intensity allows the volume of areas with low ^{131}I accumulation and their spatial distance from areas with high ^{131}I accumulation to be measured. This capability will facilitate the investigation of the impact of volume and spatial distance of areas with low ^{131}I accumulation on the overall outcome of ^{131}I therapy in patients with advanced thyroid cancer.

Conclusions

In summary, a customized mouse cradle facilitates consistent tissue configuration, such that rigid body registration can be applied to align serial images of the same mouse via in-house CTViewer software. The approach of superimposing thyroid VOIs from t24 images to select the thyroid VOI on corresponding aligned t1 images can be applied to studies in which target tissue has differential radiotracer retention from surrounding tissues. The ability to identify location with *xyz* coordinates and to measure the volume of areas with low ^{131}I accumulation allows investigators to predict response to ^{131}I therapy and to uncover novel strategies to improve ^{131}I therapeutic efficacy.

Acknowledgments

We are grateful to Dr. James Fagin at Memorial Sloan Kettering for providing the TgBRAF^{V600E} mice. We would like to thank Kevin Wolfe for sharing his expertise to help us determine the best material and resolution for 3D printing of the cradle and for printing and assembling the cradle. We would also like to thank Akram Hussein, Rodd Reinhart, and Andrew Brown for preparing the ^{123}I doses for our SPECT/CT imaging studies. This work was supported in part by National Institutes of Health (NIH) grant P01CA124570 (project 3 leader: S.M.J; PI: M.D. Ringel), NIH grant P50CA168505 (project 2 leader; S.M.J.; PI: M.D. Ringel), National Science Foundation (NSF) grant CMMI-1067962 (PI: C.H.M.), and NSF grant CMMI-1200017 (PI: C.H.M.). B.H. is a recipient of NIH/NIDCR T32 DE014320.

Author Disclosure Statement

The authors have nothing to disclose.

References

1. Mazzaferri EL, Jhiang SM 1994 Long-term impact of initial surgical and medical therapy on papillary and follicular thyroid cancer. Am J Med **97:**418–428.
2. Reiners C, Hanscheid H, Luster M, Lassmann M, Verburg FA 2011 Radioiodine for remnant ablation and therapy of metastatic disease. Nat Rev Endocrinol **7:**589–595.
3. Schlumberger M, Sherman SI 2012 Approach to the patient with advanced differentiated thyroid cancer. Eur J Endocrinol **166:**5–11.
4. Sherman SI 2011 Targeted therapies for thyroid tumors. Mod Pathol **24:**S44–52.
5. Cabanillas ME, Schlumberger M, Jarzab B, Martins RG, Pacini F, Robinson B, McCaffrey JC, Shah MH, Bodenner DL, Topliss D, Andresen C, O'Brien JP, Ren M, Funahashi Y, Allison R, Elisei R, Newbold K, Licitra LF, Sherman SI, Ball DW 2015 A Phase 2 trial of lenvatinib (E7080) in advanced, progressive, radioiodine-refractory, differentiated thyroid cancer: a clinical outcomes and biomarker assessment. Cancer **121:**2749–2756.
6. Schlumberger M, Tahara M, Wirth LJ, Robinson B, Brose MS, Elisei R, Habra MA, Newbold K, Shah MH, Hoff AO, Gianoukakis AG, Kiyota N, Taylor MH, Kim SB, Krzyzanowska MK, Dutcus CE, de las Heras B, Zhu J, Sherman SI 2015 Lenvatinib versus placebo in radioiodine-refractory thyroid cancer. N Engl J Med **372:**621–630.
7. Nagarajah J, Le M, Knauf JA, Ferrandino G, Montero-Conde C, Pillarsetty N, Bolaender A, Irwin C, Krishnamoorthy GP, Saqcena M, Larson SM, Ho AL, Seshan V, Ishii N, Carrasco N, Rosen N, Weber WA, Fagin JA 2016 Sustained ERK inhibition maximizes responses of *BrafV600E* thyroid cancers to radioiodine. J Clin Invest **126:**4119–4124.
8. Chakravarty D, Santos E, Ryder M, Knauf JA, Liao XH, West BL, Bollag G, Kolesnick R, Thin TH, Rosen N, Zanzonico P, Larson SM, Refetoff S, Ghossein R, Fagin JA 2011 Small-molecule MAPK inhibitors restore radioiodine incorporation in mouse thyroid cancers with conditional *BRAF* activation. J Clin Invest **121:**4700–4711.
9. Ho AL, Grewal RK, Leboeuf R, Sherman EJ, Pfister DG, Deandreis D, Pentlow KS, Zanzonico PB, Haque S, Gavane S, Ghossein RA, Ricarte-Filho JC, Dominguez JM, Shen R, Tuttle RM, Larson SM, Fagin JA 2013 Selumetinib-enhanced radioiodine uptake in advanced thyroid cancer. N Engl J Med **368:**623–632.
10. Knauf JA, Ma X, Smith EP, Zhang L, Mitsutake N, Liao XH, Refetoff S, Nikiforov YE, Fagin JA 2005 Targeted expression of *BRAFV600E* in thyroid cells of transgenic mice results in papillary thyroid cancers that undergo dedifferentiation. Cancer Res **65:**4238–4245.
11. Armour M, Ford E, Iordachita I, Wong J 2010 CT guidance is needed to achieve reproducible positioning of the mouse head for repeat precision cranial irradiation. Radiat Res **173:**119–123.
12. Corroyer-Dulmont A, Falzone N, Kersemans V, Thompson J, Hill M, Allen PD, Beech J, Gilchrist S, Kinchesh P, Vojnovic B, Tullis I, Gaze MN, Smart S, Vallis KA 2017 MRI-guided radiotherapy of the SK-N-SH neuroblastoma xenograft model using a small animal radiation research platform. Br J Radiol **90:**20160427.

13. Kiehl EL, Stojadinovic S, Malinowski KT, Limbrick D, Jost SC, Garbow JR, Rubin JB, Deasy JO, Khullar D, Izaguirre EW, Parikh PJ, Low DA, Hope AJ 2008 Feasibility of small animal cranial irradiation with the microRT system. Med Phys **35:**4735–4743.
14. Kim H, Fabien J, Zheng Y, Yuan J, Brindle J, Sloan A, Yao M, Lo S, Wessels B, Machtay M, Welford S, Sohn JW 2014 Establishing a process of irradiating small animal brain using a CyberKnife and a microCT scanner. Med Phys **41:**021715.
15. Haney CR, Fan X, Parasca AD, Karczmar GS, Halpern HJ, Pelizzari CA 2008 Immobilization using dental material casts facilitates accurate serial and multimodality small animal imaging. Concepts Magn Reson Part B Magn Reson Eng **33B:**138–144.
16. Kokuryo D, Kimura Y, Obata T, Yamaya T, Kawamura K, Zhang MR, Kanno I, Aoki I 2010 A small animal holding fixture system with positional reproducibility for longitudinal multimodal imaging. Phys Med Biol **55:**4119–4130.
17. Suckow C, Kuntner C, Chow P, Silverman R, Chatziioannou A, Stout D 2009 Multimodality rodent imaging chambers for use under barrier conditions with gas anesthesia. Mol Imaging Biol **11:**100–106.
18. Fricke ST, Vink R, Chiodo C, Cernak I, Ileva L, Faden AI 2004 Consistent and reproducible slice selection in rodent brain using a novel stereotaxic device for MRI. J Neurosci Methods **136:**99–102.
19. Segars WP, Tsui BM, Frey EC, Johnson GA, Berr SS 2004 Development of a 4-D digital mouse phantom for molecular imaging research. Mol Imaging Biol **6:**149–159.
20. Kesner AL, Dahlbom M, Huang SC, Hsueh WA, Pio BS, Czernin J, Kreissl M, Wu HM, Silverman DH 2006 Semiautomated analysis of small-animal PET data. J Nucl Med **47:**1181–1186.
21. Khmelinskii A, Groen HC, Baiker M, de Jong M, Lelieveldt BP 2012 Segmentation and visual analysis of whole-body mouse skeleton microSPECT. PLoS One **7:**e48976.
22. Gutierrez DF, Zaidi H 2012 Automated analysis of small animal PET studies through deformable registration to an atlas. Eur J Nucl Med Mol Imaging **39:**1807–1820.
23. Saeedzadeh E, Sarkar S, Abbaspour Tehrani-Fard A, Ay MR, Khosravi HR, Loudos G 2012 3D calculation of absorbed dose for 131I-targeted radiotherapy: a Monte Carlo study. Radiat Prot Dosimetry **150:**298–305.

Address correspondence to:
Sissy M. Jhiang, PhD
Department of Physiology and Cell Biology
The Ohio State University
304 Hamilton Hall
1645 Neil Avenue
Columbus, OH 43210

E-mail: Jhiang.1@osu.edu

Chia-Hsiang Menq, PhD
Department of Mechanical and Aerospace Engineering
The Ohio State University
W394 Scott Lab
201 W 19th Avenue
Columbus, OH 43210

E-mail: menq.1@osu.edu